SIMULATION OF AN UAV WITH INTERMESHING ROTORS USING THE LATTICE-BOLTZMANN METHOD

Andreas Reiser
Graduate Research Assistant

Ilkay Yavrucuk
Professor and Department Head

Institute of Rotorcraft and Vertical Flight
Technical University of Munich
Munich, Germany

ABSTRACT

This paper presents a validation study of a mid-fidelity simulation framework for rotorcraft aeromechanics, applied to an unmanned aerial vehicle with an intermeshing rotor configuration. The framework couples a rigid-body multibody dynamics model with a Lattice-Boltzmann Method (LBM) fluid solver, using an Actuator Line Model (ALM) for rotor representation. Validation is performed across three configurations: isolated single-rotor testing, full-scale hover flight at multiple altitudes, and trimmed forward flight. Simulation results for rotor thrust, power, torque, and control inputs are compared against experimental data. The framework is shown to capture key aerodynamic and control trends, with some underprediction of power and torque in transitional forward flight. These results support its suitability for simulating complex rotor-rotor interactions in intermeshing rotorcraft and inform future model refinements.

NOMENCLATURE

A	Rotor disk area, $= \pi R^2$, m^2
c	Rotor blade chord length, m
C_T	Rotor thrust coefficient, $= T/\rho A(\Omega R)^2$
C_P	Rotor power coefficient, $= T/\rho A(\Omega R)^3$
M_{tip}	Rotor blade tip mach number
N_b	Number of rotor blades
r	Radial distance from rotational axis, m
r_a	Root cutout, m
R	Rotor radius, m
S	Area, m^2
t	Time, s
T	Rotor thrust, N
V_{tip}	Rotor blade tip velocity
β_0	Precone angle, deg
Δx	LBM grid spacing, m
Δz	Axial spacing, m
ε	isotropic Gaussian kernel size for ALM, m
ε_c	chord-wise kernel size, m
ε_t	thickness-wise kernel size, m
ε_r	kernel size in radial direction, m
ω	Vorticity, s^{-1}
Ω	Angular velocity of the rotor, $\mathrm{rad\,s^{-1}}$
ψ_b	Rotor blade azimuth angle, deg
ϕ	Azimuthal spacing (index angle), deg
ρ	Air density, $\mathrm{kg\,m^{-3}}$
σ	Rotor solidity $= N_b c/(\pi R)$
θ_0	Collective pitch angle, deg
ARCS	Flight mechanics code of HT
AREA	Autonomous Rotorcraft for Extreme Altitudes
ALM	Actuator Line Model
HT	Institute of Rotorcraft and Vertical Flight
LBM	Lattice Boltzmann Method
MSL	Mean Sea Level

INTRODUCTION

Modeling rotorcraft aerodynamics with high accuracy remains a central challenge, particularly for configurations involving multiple, interacting rotors. Intermeshing rotor systems, also known as synchropters, introduce significant complexity due to strong rotor-rotor interference, non-uniform inflow, and unsteady wake coupling. Traditional low-order models often lack the fidelity to resolve these effects, while high-fidelity blade-resolved CFD remains computationally prohibitive for many applications.

Mid-fidelity approaches, such as those using actuator-based methods embedded in field solvers, offer a balance between realism and efficiency. In this context, the Actuator Line Model (ALM) combined with a Lattice-Boltzmann Method (LBM) flow solver enables efficient simulation of unsteady wake dynamics in three-dimensional domains, leveraging GPU acceleration for practical runtimes. The approach has seen success in wind energy and rotorcraft applications and is extended here to an intermeshing rotor UAV configuration.

This paper applies a previously validated simulation framework (Ref. 1) to the Autonomous Rotorcraft for Extreme Altitudes (AREA), an electrically powered UAV with two intermeshing rotors. The study evaluates the predictive performance of the framework in single-rotor tests, hover at multiple altitudes, and forward flight. Comparison with experimental data focuses on thrust, power, torque, and trim behavior.

THE AREA UAV

(a) AREA in flight.

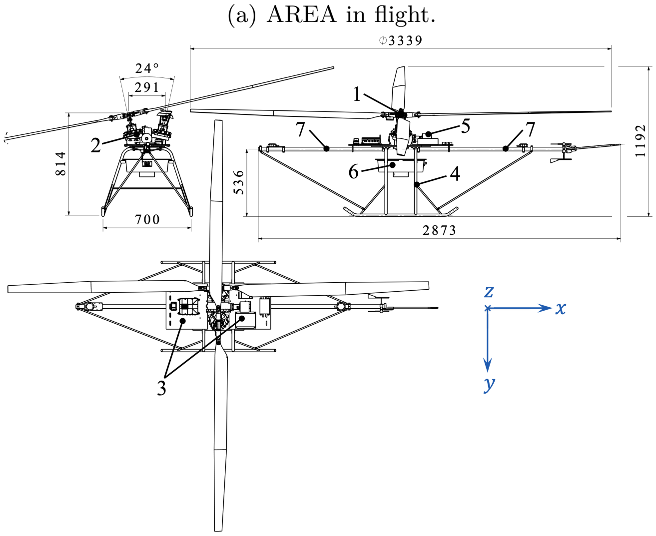

(b) Three-view orthographic projection of AREA.

Figure 1. The AREA UAV. Pictures taken from (Ref. 2).

The AREA is an electrically powered, unmanned helicopter developed at the Institute of Helicopter Technology (HT) at the Technical University of Munich (TUM) for research in high-altitude rotorcraft operations. The vehicle employs a twin two-bladed intermeshing rotor configuration, also known as a Flettner or synchropter layout, which eliminates the need for a tail rotor by achieving torque balance through contra-rotation. This configuration provides compactness, high control authority, and aerodynamic efficiency in hover, making it particularly suitable for operation in low-density environments at altitudes up to 9000 m.

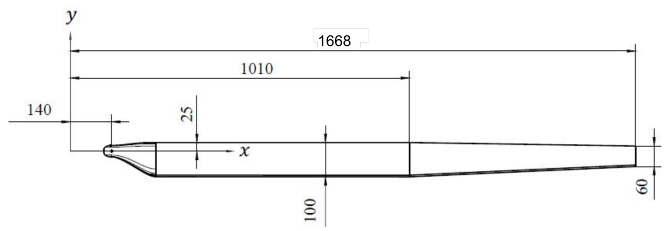

Figure 2. AREA blade dimensions. Schematic taken from (Ref. 3).

The rotor system is composed of two teetering rotor heads, canted outward by 12°, and synchronized through a gearbox to maintain a fixed azimuthal phase difference between the blades. Each rotor blade features a NACA 23012 airfoil, linear taper and twist, and is constructed from carbon fiber with a foam core and integrated lead mass for chordwise balancing, see Figure 2. Control is achieved via independent swashplates for each rotor, allowing for differential cyclic inputs to generate pitch, roll, and yaw moments. Rotor hub flapping is damped elastomerically, and the lag motion is controlled via friction hinges.

Originally powered by a battery-electric drivetrain, the UAV is designed around a single electric motor driving both rotors via a two-stage gearbox. The system architecture supports comprehensive instrumentation, including rotor blade root bending moment sensors and strain gauges for torque and flap moment measurement, which were used during extensive hover, climb, and forward flight test campaigns. Data collected from these campaigns have been used to inform the sizing of a hydrogen fuel cell-based propulsion system, aimed at extending the vehicle's endurance beyond the original 20–25 minute battery constraint (Ref. 4). Flight tests with the hydrogen fuel cell-based propulsion system are currently ongoing.

Originally, flight tests were conducted in free-air, out-of-ground-effect conditions at an altitude of approximately 510m and 2800m MSL. Measurements included air data, GPS position, inertial motion, battery and motor performance, and rotor dynamics. Key rotor quantities, such as torque and flap moment, were acquired using strain gauges mounted directly on the rotating components, with data synchronized across the rotating and fixed frames. Angular rate stabilization was active, but pilot inputs were manual. Data segmentation was performed post-flight using synchronized control commands and power transients, followed by automated flight state detection. Standard deviations in measured parameters such as rotor power remained within ±120 W in hover and climb, indicating high signal consistency and measurement accuracy suitable for performance validation (Refs. 2, 5).

Given its well-characterized geometry, low disc loading, and tightly coupled aerodynamic and dynamic behavior, the AREA serves as an ideal benchmark vehicle for evaluating mid-fidelity rotorcraft simulation frameworks. In particular, the intermeshing rotor configuration introduces strong flap-lag coupling and tip-path-plane interference effects that are not trivially modeled with linear inflow approximations.

MERIT: ROTOR TEST RIG

The MERIT rotor test rig, also designed and built at HT, enables Mach-scaled testing of single rotors with high-resolution thrust and power measurement. Its rigid, hingeless hub and precise instrumentation provide a clean aerodynamic environment ideal for validating isolated rotor performance. While there is photogrammetry equipment in place to capture blade deformations, those data are not utilized in this study.

As a first step in validating the simulation framework used in this work, the AREA rotor blades were tested on MERIT in a single-rotor setup, see Figure 3. A series of collective pitch and rotor speed sweeps were conducted to generate baseline thrust and power data. Due to differences in hub geometry, the mounted blades resulted in a 54 mm larger rotor radius compared to the original AREA UAV configuration. This adaptation is accounted for in the simulation.

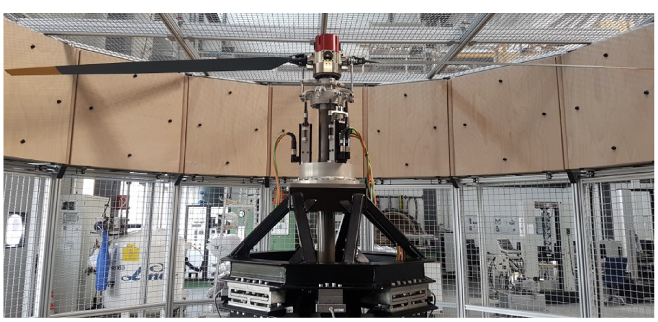

Figure 3. AREA rotor blades mounted on MERIT test rig. Picture taken from (Ref. 3).

METHODOLOGY

The aircraft's kinematics are modeled by ARCS, a solver based on a general-purpose rigid multibody formulation capable of representing arbitrary rotor and fuselage configurations. Swashplate mechanisms, as well as drivetrain dynamics are not modeled. Blade aerodynamic loads are computed using blade element momentum theory, with pitch angles prescribed directly at the blade root hinge. These loads are coupled in time with a GPU-accelerated LBM solver that resolves the unsteady three-dimensional flow field. At each timestep, inflow velocities are sampled from the LBM grid and used by ARCS to compute sectional forces, which are then projected back into the fluid domain.

In addition to load coupling, the framework optionally supports full six-degree-of-freedom coupling of the vehicle's motion to the LBM solver using an Arbitrary Lagrangian-Eulerian (ALE) formulation. This allows simulation of trimmed flight and transient maneuvers with dynamic interaction between vehicle motion and surrounding flow.

The framework and its numerical parameters follow those validated in previous work by the authors (Ref. 1).

Actuator Line Model

Rotor blades are modeled as distributed force elements along their span. The aerodynamic forces are projected onto the flow domain using a non-isotropic Gaussian kernel as proposed by Churchfield et al. (Ref. 6), improving upon the original isotropic formulation by Sørensen and Shen (Ref. 7). The projection distributes each sectional force $\vec{F}$ over the fluid volume via a three-dimensional Gaussian function defined in blade-aligned coordinates - chordwise (x_c), thickness (x_t), and spanwise (x_r) - as:

$$g_{AAL}(x_c, x_t, x_r) = \frac{1}{\varepsilon_c \varepsilon_t \varepsilon_r \pi^{3/2}} \exp\left(-\frac{(x_c - x_{0,c})^2}{\varepsilon_c^2} - \frac{(x_t - x_{0,t})^2}{\varepsilon_t^2} - \frac{(x_r - x_{0,r})^2}{\varepsilon_r^2}\right) \quad (1)$$

Here, $(x_{0,c}, x_{0,t}, x_{0,r})$ define the actuator point location in the local coordinate system, and ε_c, ε_t, and ε_r are the kernel widths in each direction. The Gaussian kernel smooths the body-force projection, mitigating numerical instabilities and allowing for pitch and twist variation along the blade.

Following the results in (Ref. 1), the kernel widths are selected as:

$$\varepsilon_c = \varepsilon_t = 2\Delta x$$
$$\varepsilon_r = \Delta x$$

Table 1. Technical specifications for the AREA UAV. Reproduced from (Ref. 2).

Parameter	Unit	Value
Number of rotors N_R	1	2
Number of blades per rotor N_{Rb}	1	2
Rotation direction (right; left)	-	CW; CCW
Azimuthal angle separation ϕ_{Az}	°	90
Tilt (right; left) about x | y	°	12; -12 | 0; 0
Position (right; left) in x | y | z	m	0; 0 | 0.15; -0.15 | -0.24; -0.24
Airfoil	-	NACA 23012 with tab
Rotor radius R	m	1.668
Cone angle ϕ_K	°	0
Linear twist θ_{tw}	°	-10
Start of aerodynamic profile r_{ae}	m	0.27
Chord length c at $r = 0.16 \mid 0.6 \mid 1.0$	m	0.1 | 0.1 | 0.06
Nominal tip speed $V_{tip,nom}$	m/s	120
Horizontal drag area $C_D S$	m^2	0.35
Rotor hub type	-	Teeter
Radial position of lag hinge r_{LH}	m	0.14
Nominal take-off weight M	kg	36.6
Maximum take-off weight $MTOW$	kg	56.6
Center of gravity position $x_{CG} \mid y_{CG} \mid z_{CG}$	m	0.017 | 0 | 0.029
Moment of inertia (M = 36.6 kg) $J_{xx} \mid J_{yy} \mid J_{zz}$	$\mathrm{kg} \cdot \mathrm{m}^2$	5 | 7.2 | 9.3

Inflow Sampling

The inflow velocity at each actuator point is sampled using the same non-isotropic Gaussian kernel employed for force projection, as proposed by Forsythe et al. (Ref. 8) and further supported by Churchfield et al. (Ref. 6). This approach avoids ad-hoc placement of sampling points and eliminates tunable parameters, which is particularly beneficial when blades operate in highly non-uniform or vortical flows, as seen in intermeshing rotor systems.

Tip Correction

Blade tip effects are accounted for using a smooth, analytic tip loss factor that suppresses lift near the blade tip, compensating for the absence of full 3D vortex resolution in the blade element formulation. This method is also employed in by DYMORE (Ref. 9). The tip loss factor is given by:

$$C_{\mathrm{TL}} = \tanh\left(\frac{1-r}{1-l}\right) \quad (2)$$

$$C_{\mathrm{TL},\%} = 1 - \int_{\mathrm{r}=0}^{1} \tanh\left(\frac{1-r}{1-l}\right) \mathrm{d}r \quad (3)$$

where r is the normalized radial coordinate and l is the tuneable parameter. l varies in theory from 0-1 and is, in reality, often between 0.93 and 0.97. In this paper, all simulations use $l = 0.95$, which results in a percent reduction of thrust of $\sim 3.5\%$ using Equation 3.

In theory, with sufficiently high grid resolution, the actuator line projection in LBM could resolve the tip vortex core without additional correction, and will be part of future investigations. However, due to computational cost constraints, the LBM resolution in this study is limited to 128 cells per rotor radius. At this resolution, the tip vortices are excessively diffuse and over-predict their core size, which leads to under-resolved blade tip aerodynamics. Therefore, the use of a tip loss correction remains necessary to reproduce realistic thrust and power distributions.

Aircraft Trimming

To establish trimmed flight conditions across hover and forward flight regimes, an iterative trimming algorithm was employed based on a precomputed Jacobian matrix. The objective of the trim procedure was to determine the set of steady-state control inputs that minimized the net forces and moments at the vehicle center of gravity.

The six trim variables included the four conventional pilot controls along with the prescribed fuselage pitch and roll angles:

$$\mathbf{u} = \left[\theta_{\mathrm{lon}}, \theta_{\mathrm{lat}}, \theta_{\mathrm{col}}, \theta_{\mathrm{ped}}, \theta, \phi\right] \quad (4)$$

These inputs were mapped to the resulting force and moment vector at the CG, expressed in the body-fixed frame:

$$\mathbf{F}_{\mathrm{CG}} = \left[X, Y, Z, L, M, N\right] \quad (5)$$

The Jacobian matrix $\mathbf{J} \in \mathbb{R}^{6\times6}$ is computed offline using finite-difference perturbations about a nominal operating point:

$$\mathbf{J}_{ij} = \frac{\partial (\mathbf{F}_{\mathrm{CG}})_i}{\partial \mathbf{u}_j} \tag{6}$$

To improve robustness and reduce the influence unsteady aerodynamic effects, a second-order Butterworth low-pass filter was applied to the raw simulated forces and moments prior to residual evaluation. This filtering step ensured repeatable and stable convergence during the trimming process.

At each iteration k, the residual force/moment vector was computed from the filtered data:

$$\mathbf{r}_k = \mathbf{F}_{\mathrm{CG},k} \tag{7}$$

and the control vector was updated using the inverse Jacobian:

$$\mathbf{u}_{k+1} = \mathbf{u}_k - \mathbf{J}^{-1}\mathbf{r}_k \tag{8}$$

Trim convergence was achieved when the magnitude of the residual vector fell below a specified threshold:

$$\|\mathbf{r}_k\|_2 < 1 \tag{9}$$

This iterative method provided a reliable and computationally efficient means of determining trimmed flight states, supporting validation in both hover and forward flight configurations.

SIMULATION SETUP

The AREA is modeled in ARCS based on the parameters given in Table 1. 128 blade elements are used for each blade. The LBM fluid dynamic component of the simulation framework uses a D3Q19 lattice descriptor. The computational domain is defined as a cube with side lengths equal to six times the rotor radius (6R), providing sufficient space for wake development and minimizing spurious boundary interactions. All domain boundaries are treated as free-outflow conditions using an impedance-based boundary formulation, which effectively attenuates non-physical wave reflections in unsteady aerodynamic and aeroacoustic simulations, see (Ref. 10). The aircraft model is centered within the domain such that the rotor disk planes are located at the geometric center. Rotor blades are modeled using an advanced actuator line method (ALM), which enables realistic representation of blade-induced momentum and vorticity without the computational expense of resolving blade geometry directly. The fuselage and rotor hub are approximated using simplified geometrical volumes to account for gross flow blockage effects. These structures do not contribute to the calculation of aerodynamic forces and serve solely to alter the local flow field. To enhance computational efficiency while preserving resolution in critical regions, hierarchical grid refinement is employed. The finest grid region, responsible for resolving rotor near-wake and tip vortex structures, occupies the central volume with sidelength equal to half the total domain size. Grid resolution coarsens progressively toward the outer domain boundaries. An XZ-plane slice of the computational domain is shown in Figure 4, where the grayscale colormap indicates resolution in terms of cells per rotor radius. The pink geometry at the center represents the simplified fuselage and rotor hub components.

Table 2. LBM simulation parameters.

LBM Parameter	Value
Domain size	6x6x6 radii
Refinement levels	2
Refined domain size	3x3x3 radii
Refined resolution	128 [cells/radius]
Refined Δx	0.013 [m]
Timestep Δt	0.025 [ms]
Number of GPUs	8 A100

Figure 4. XZ slice of LBM computational domain. Gray scale represents resolution in terms of cells per radius. The finest grid in the center has sidelengths half the size of the full domain. Pink structure in the middle represents simplified fuselage and rotor hub geometry.

All simulations use identical LBM solver parameters. A summary of these parameters is provided in Table 2.

For forward flight trim simulations, the framework employs an Arbitrary Lagrangian-Eulerian (ALE) formulation to enable free movement of the computational domain, based on (Ref. 11). While the aircraft remains stationary relative to its local LBM grid, the entire domain is translated and rotated within a larger, pre-computed external flow field according to the aircraft's six-degree-of-freedom motion. This ALE implementation permits both translational and rotational motion of the domain without deforming the underlying Cartesian grid, ensuring consistency with the LBM solver's requirements. At each time step, the domain's position and orientation are updated based on the current aircraft state, and flow quantities at the domain boundaries are interpolated from the external field, which in this study is a zero velocity external field. This approach was extensivley used and validated in (Ref. 12) and (Ref. 13). Figure 5 shows the volume representation of the vorticity magnitude for trimmed forward flight at 10 m/s.

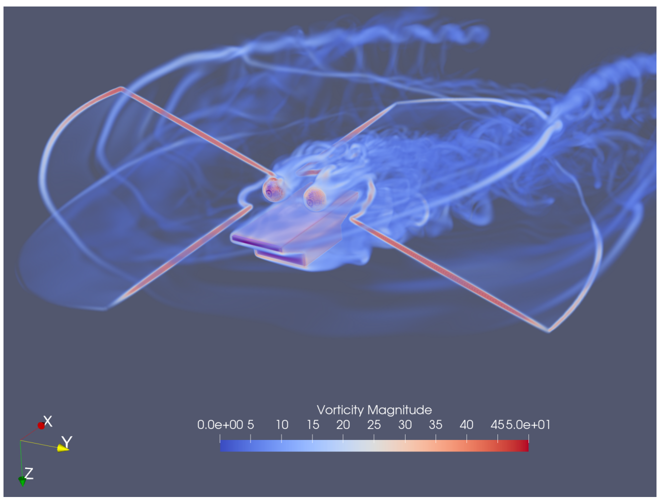

Figure 5. Volume representation of vorticity magnitude for 10 m/s trimmed forward flight.

In terms of computational cost, the baseline non-ALE setup, such as a single rotor hover simulation using a domain size of 6R and a central grid resolution of 128 cells per rotor radius, requires approximately 3 minutes of wall-clock time per physical second of simulation when executed on 8 NVIDIA A100 GPUs. When the ALE formulation is used to enable full six-degree-of-freedom domain motion, the computational time increases by roughly a factor of two. This increase is primarily due to the additional overhead from interpolation and remapping operations at each time step. The still relatively low computation time, even with ALE, makes the analysis of transient flight maneuvers feasible within practical turnaround times. Reaching a trimmed flight condition using the method described in the previous section typically requires about 3 seconds of simulation time, including a initial rotor speed ramp-up phase.

RESULTS AND DISCUSSION

Test Rig: Single Rotor

Figure 6 presents a comparison between experimental measurements and simulation results for rotor power consumption and thrust generation. The data cover a range of collective pitch angles at rotational speeds of 600 and 800 RPM. Simulation results were obtained using the ARCS+LBM framework, while the experimental data were collected using a single-rotor test rig operating at an ambient air density of 1.159 kg/m^3.

The power values shown represent the aerodynamic power required to drive the rotor blades. In the experiment, parasitic losses associated with the shaft, hub, blade attachments, and bearing friction were measured separately by operating the test rig without blades. These losses were subtracted from the total measured input power to isolate the aerodynamic component. The simulation model does not include these mechanical losses and accounts only for blade aerodynamics.

The simulation captures the general trend in both power and thrust. However, at higher rotational speeds and collective pitch angles, it underpredicts the absolute power values. Despite this discrepancy, the ARCS+LBM framework demonstrates good agreement with the experimental data and reproduces the key aerodynamic characteristics of the single-rotor system.

Flight Test: Hover

To further validate the simulation framework, hover flight performance of the full-scale UAV was investigated. The vehicle employs an intermeshing rotor configuration, and it is a reasonable assumption that, in symmetric hover, both rotors contribute equally to total thrust and power. As such, the results are presented on a per-rotor basis for direct comparison with the single-rotor simulation model.

Hover tests were conducted using the AREA at five discrete tip speeds ranging from approximately 100 m/s to 140 m/s. For each tip speed, five thrust levels were tested, resulting in a well-distributed test matrix covering the relevant hover flight envelope. Weight was added to achieve the desired thrust loading per rotor.

Due to the intermeshing rotor configuration, the two rotor shafts are tilted and seperated by an angle of 24 degrees relative to each other. This arrangement with the different directions of rotation produces a net nose-up pitching moment about the aircraft's lateral (y) axis. As rotor thrust - and thus torque - increases, this nose-up moment becomes more pronounced. To counteract this effect and avoid the need for longitudinal cyclic input during hover, the center of gravity was intentionally positioned forward of the rotor hub centers. This CG offset generates a passive nose-down pitching moment that

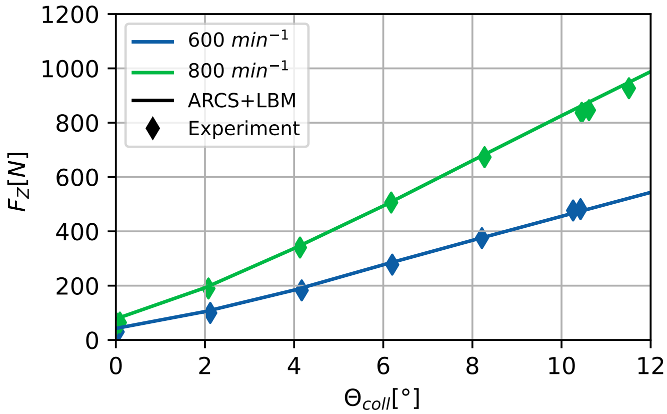

(a) Thrust.

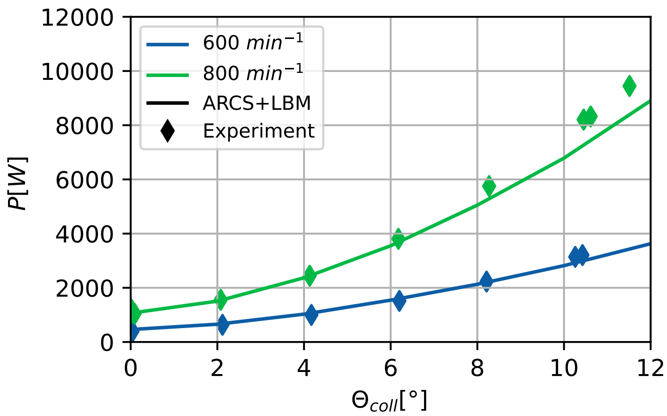

(b) Power.

Figure 6. Comparison of calculated thrust and power to experimental data for collective sweep at 600 and 800 RPM.

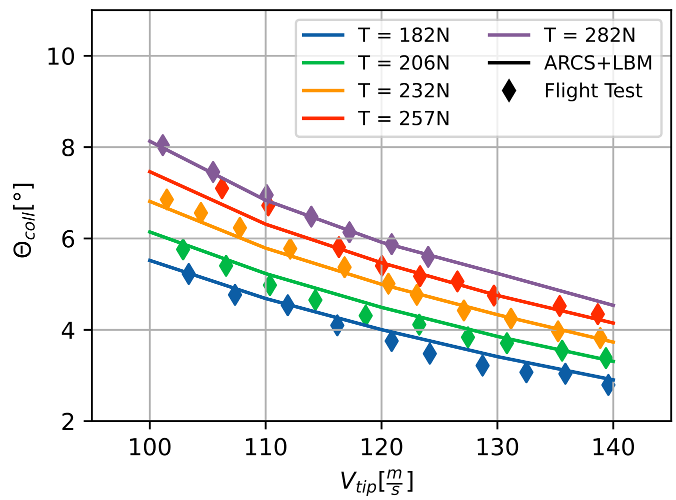

(a) 500 m MSL

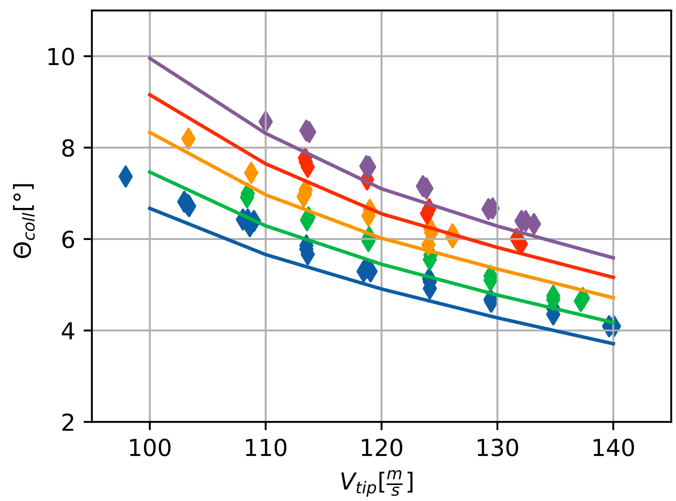

(b) 2800 m MSL

Figure 7. Comparison of calculated collective angle to flight test data for different thrust levels and tip speeds at different altitudes.

precisely balances the rotor-induced torque. For each flight condition, the CG was adjusted accordingly, ensuring that stable, trimmed hover flight could be achieved with collective pitch input alone.

Tests were performed at two altitudes: 500 m MSL and 2800 m MSL. Atmospheric measurements indicated ISA + 5 °C conditions at both sites. The resulting air density, speed of sound, and kinematic viscosity were incorporated into the simulation to ensure matching environmental conditions.

Figure 7a and 7b show the measured and simulated collective pitch angles required to achieve each thrust level as a function of tip speed, at low and high altitude respectively. At both test altitudes, the ARCS+LBM simulation framework demonstrates good agreement with experimental results. The collective pitch required to maintain hover decreases with increasing tip speed, consistent with expectations from rotor theory. The simulation captures this trend accurately across all thrust levels. Minor but consistent underprediction of collective pitch is observed at higher thrust settings and lower tip speeds, particularly at 2800 m MSL.

Figure 8a and 8b show the corresponding power requirements for a single rotor at 500 m and 2800 m MSL, respectively. The simulation results are generally in good agreement with the flight test data, capturing the slope and expected increase in power with both tip speed and thrust. At 500 m MSL, the simulation slightly underpredicts power at higher tip speeds for the two highest thrust levels, while matching well at lower thrusts and lower tip speeds. At 2800 m MSL, the simulation consistently underpredicts the measured power across the entire test matrix. Despite these discrepancies, the overall trends are well captured, and the simulation provides a reasonable approximation of power requirements for the intermeshing rotor system in hover flight under varying environmental conditions.

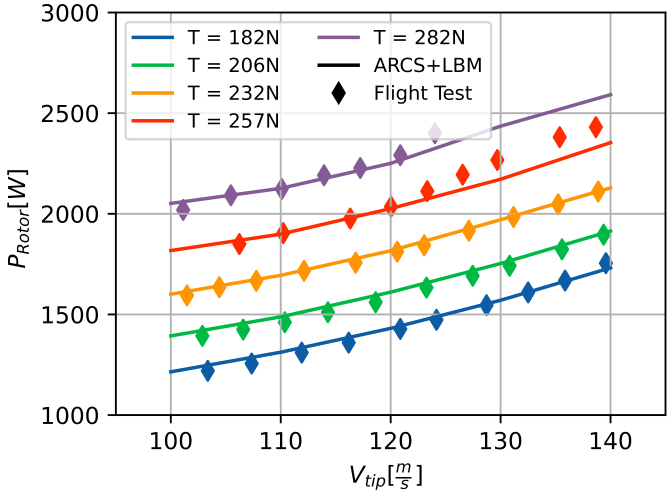

(a) 500 m MSL

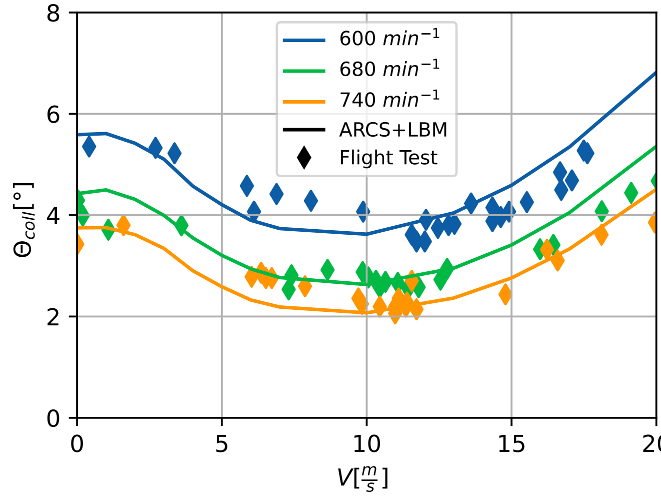

(a) collective

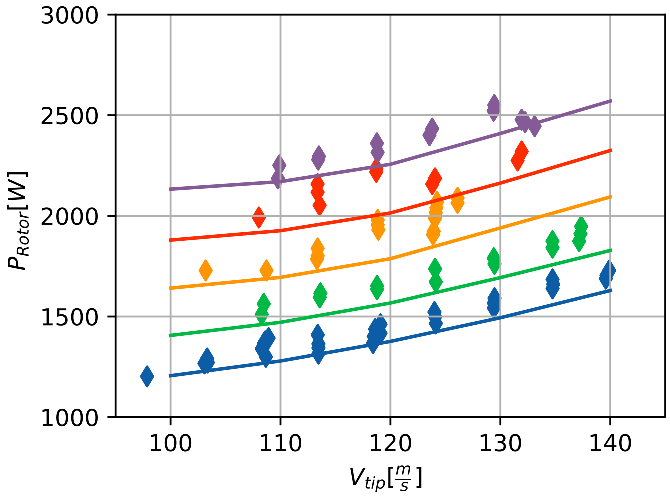

(b) 2800 m MSL

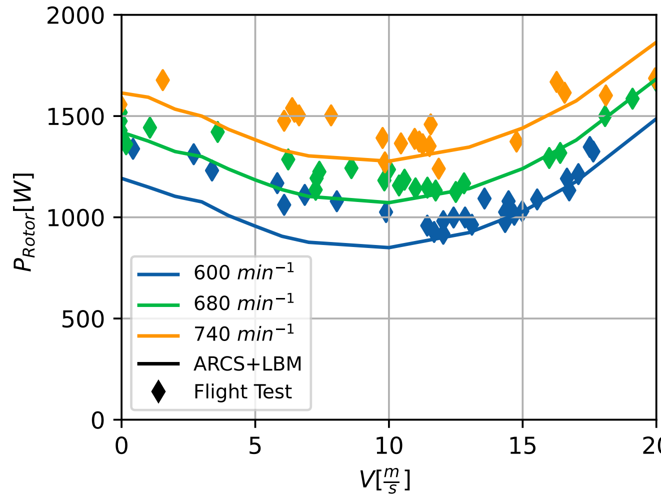

(b) power

Figure 8. Comparison of required single rotor power to flight test data for different thrust levels and tip speeds at different altitudes.

Figure 9. Comparison of calculated power and collective angle in forward flight to flight test data for different rotor speeds.

Flight Test: Forward Flight

The forward flight simulations were performed at nominal takeoff weight (36.6 kg) and 500 m MSL, using the previously described simulation setup and trimming methodology. The results investigate the vehicle's trimmed behavior at three different rotor speeds - 600 RPM, 680 RPM , and 740 RPM for forward speeds up to 20 m/s. The ARCS+LBM simulation results are compared to corresponding flight test data. Note, that cyclic lateral and pedal inputs remain close to zero for all investigated forward flight conditions.

Figure 9a and 9b show the required collective pitch angle and single rotor power respectively. The collective pitch angle response in forward flight shows a consistent trend across all tested rotor speeds. From hover up to approximately 3 m/s, the collective remains nearly constant. As forward speed increases beyond this point, the collective decreases, reaching a minimum around 10–12 m/s, and then increases slightly again at higher speeds (15–20 m/s). This behavior reflects the increased rotor efficiency due to translational lift in low to moderate forward flight. Although the thrust requirement remains approximately constant to maintain level flight, improved inflow conditions reduce the rotor torque and power demand, allowing for a reduction in collective pitch. At higher forward speeds, rising parasitic and profile drag forces require additional thrust, leading to a corresponding increase in collective.

The simulation reproduces these trends well and aligns closely with the flight test data across all rotor speeds. Minor discrepancies are observed at higher speeds (>15 m/s), where the simulation overpredicts the collective pitch for the 600 RPM and 680 RPM cases. The power required per rotor during forward flight follows the expected trend for rotorcraft operating at constant altitude. For all three rotor speeds required power initially decreases with forward speed, reaches a minimum near 10–12 m/s, and then increases again at higher speeds due to rising profile and parasitic drag forces.

In comparison to flight test data, the simulation underpredicts power consumption up to approximately 12 m/s for all rotor speeds. At speeds beyond 12 m/s, the agreement between simulation and test data improves. This indicates that the simulation captures the increasing drag and associated power rise at higher airspeeds reasonably well. Overall, while the qualitative trends are well represented, the consistent underprediction at lower speeds highlights an area for further refinement in the induced power and inflow modeling during transitional forward flight.

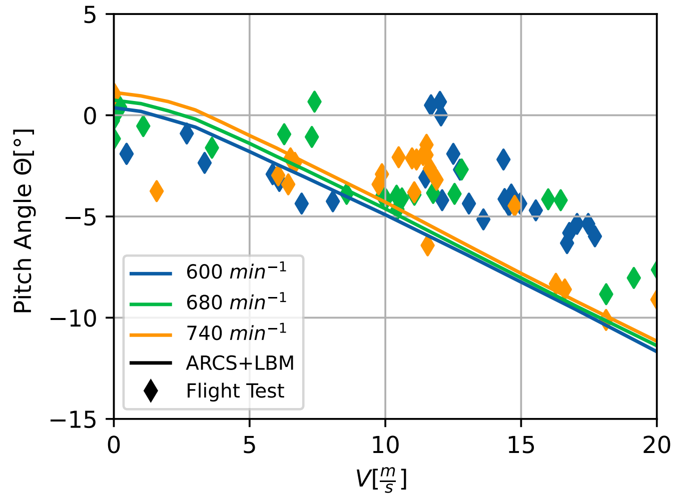

(a) aircraft pitch angle.

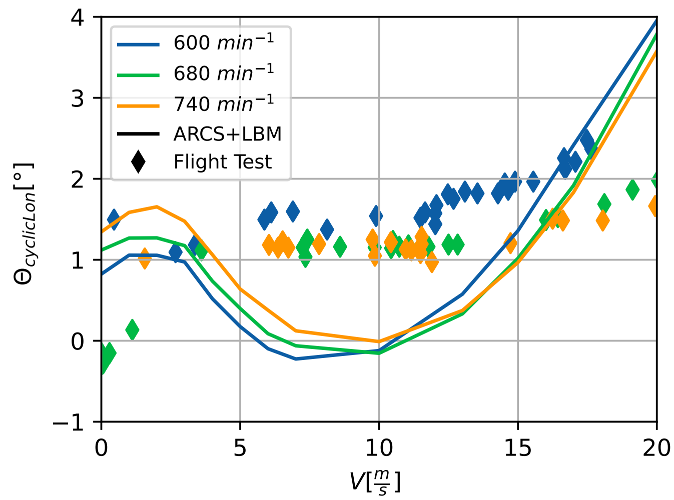

(b) cyclic longitudinal.

Figure 10. Comparison of calculated pitch angle and longitudinal cyclic in forward flight to flight test data for different rotor speeds.

Figure 10a and 10b show fuselage pitch angle and required longitudinal cyclic input respectively. The pitch angle exhibits a decreasing trend for all three rotor speeds with slight nose-up attitude at low speeds transitioning to an expected nose-down orientation at higher forward velocities. The simulation results for pitch angle are nearly identical across the three rotor speeds, indicating that rotor RPM has a minor effect on the trimmed aircraft attitude in forward flight for this configuration. Compared to flight test data, the simulated pitch angle trend is somewhat steeper. However, the flight test data show significant variability, with notable spread across the forward speed range. Despite the steeper trend in the simulation, the general behavior and magnitude of the pitch angle are well captured, particularly at higher speeds. The result demonstrates that the simulation accurately predicts the primary attitude transitions in forward flight.

In the flight test data, the cyclic input remains nearly constant at slightly above 1° up to approximately 12 m/s. Beyond this speed, the cyclic input increases gradually, with a more pronounced rise for the 600 RPM case compared to 680 and 740 RPM. Notably, the test data show nonzero cyclic input at hover and low speeds, as well as some scatter - particularly at low forward speeds. This suggests that the center of gravity was not trimmed such that zero cyclic corresponds to hover, leading to small but consistent longitudinal control offsets in the flight data. The simulation results show a distinct trend. The cyclic input begins near 1° in hover, increases slightly with speed, then decreases to near 0° or slightly negative values around 8 m/s. Following this, the cyclic input increases rapidly with forward speed, reaching the 4° limit at 20 m/s. This non-monotonic behavior, especially the reduction and reversal of cyclic at mid-speed, is not observed in the flight test and indicates a modeling discrepancy in the simulation.

One plausible explanation for this discrepancy is linked to the underprediction of power, and consequently rotor torque, as observed in the simulation up to approximately 12 m/s. This trend is mirrored in the rotor torque data shown in Figure 11, where the simulated torque values are consistently lower than those measured in flight tests for all rotor speeds up to 12 m/s.

Rotor torque contributes a residual nose-up pitching moment due to the configuration and thrust line of the intermeshing rotors. When the simulation underpredicts this torque, it simultaneously underrepresents the associated pitching moment. To maintain the correct pitch attitude - particularly given that fuselage pitch matches flight test trends fairly well - the simulation must compensate for this missing nose-up moment by reducing the longitudinal cyclic input. This compensation manifests as a reduction, and even slight reversal, of cyclic input at mid-speed flight regimes, producing the non-monotonic behavior not seen in the experimental data.

As forward speed increases beyond 12 m/s and the sim-

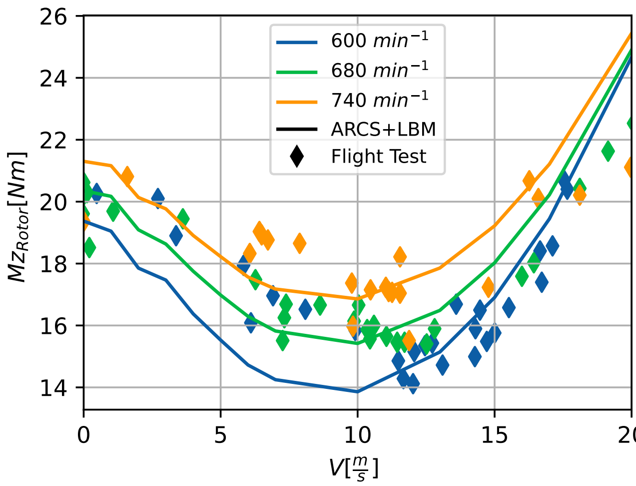

Figure 11. Comparison of calculated single rotor torque in forward flight to flight test data for different rotor speeds.

ulated torque begins to match flight values more closely, the residual pitching moment recovers, and the cyclic input trend aligns more with expectations - i.e., increasing with forward speed to tilt the rotor disk for propulsion. This highlights how tightly coupled the torque and longitudinal trim dynamics are in this configuration.

Another likely contributor to the observed non-monotonic behavior in the simulated longitudinal cyclic input is the simplified modeling of fuselage aerodynamics - specifically, the use of only a flat plate drag area to estimate parasitic drag forces. While this approach can capture first-order drag effects, it neglects the fuselage's contribution to aerodynamic pitching moments.

As reported by Barth in (Ref. 2), the fuselage of the investigated UAV configuration produces a nose-up pitching moment at angles of attack up to approximately $-10°$, transitioning to a nose-down moment at more negative angles. This aerodynamic moment, which arises from the fuselage shape and its interaction with the incoming flow, is not currently represented in the simulation due to the absence of reliable lookup tables or empirical data for fuselage moment coefficients across angle of attack.

As a result, the simulation lacks a key stabilizing moment source in forward flight, particularly in the moderate speed range where the fuselage is still operating at angles of attack associated with a nose-up contribution. This leads to the artificial reduction in cyclic input observed around 8 m/s, as the simulation compensates for the missing nose-up moment that would otherwise assist in maintaining the pitch attitude.

Together with the underpredicted rotor torque and associated residual pitching moment, the absence of fuselage moment modeling compounds the deviation in cyclic behavior. These limitations highlight the need for improved aerodynamic characterization of the fuselage - either through high-fidelity CFD simulations or wind tunnel data - to accurately capture its contribution to longitudinal trim and control requirements.

CONCLUSIONS

1. The mid-fidelity simulation framework employing a coupled LBM-ALM approach with rigid-body flight dynamics accurately captured key aerodynamic characteristics of an intermeshing rotor UAV across hover and forward flight regimes.

2. Simulated thrust and power for isolated single-rotor tests showed good agreement with experimental data, validating the actuator line modeling and aerodynamic force projection used in the framework.

3. In full-scale hover and forward flight, the simulation reliably reproduced collective pitch and power trends, though consistent underprediction of torque and power was observed at low to moderate forward speeds.

4. The study confirms the applicability of the proposed method for modeling complex rotor-rotor interactions in intermeshing configurations, and highlights the need for improved aerodynamic modeling of the fuselage enhance longitudinal trim prediction in transitional flight for this particular aircraft configuration.

Author contact:
Andreas Reiser M.Sc., andreas.reiser@tum.de
Prof. Dr. phil. Ilkay Yavrucuk, ilkay.yavrucuk@tum.de

REFERENCES

1. Reiser, A., and Yavrucuk, I., "Investigation Of Rotor Interactional Aerodynamics Using The Lattice Boltzmann Method," Proceedings of the Vertical Flight Society 80th Annual Forum, May 2024. DOI: 10.4050/F-0080-2024-1267.

2. Barth, A. U., Auslegung, Simulation, Bau und Flugerprobung eines unbemannten, elektrischen Hubschraubers mit kämmenden Rotoren für extreme Flughöhen, Ph.D. thesis, Technische Universität München, 2020.

3. Heuschneider, V., Berghammer, F., Pflumm, T., and Hajek, M., "DEVELOPMENT AND INITIAL HOVER TESTING OF THE MACH SCALED ROTOR TEST RIG MERIT," , 2021.

4. Technical University of Munich, Zappek, V., and Yavrucuk, I., "Fuel Cell Sizing for a UAV with Intermeshing Rotors using a Genetic Algorithm for NDARC Rotor Performance Calibration," Proceedings of the Vertical Flight Society 79th Annual Forum, May 2023. DOI: 10.4050/F-0079-2023-17998.

5. Technical University of Munich, Barth, A., German Aerospace Center, Kondak, K., Spieß, C., and Hajek, M., “Design, Analysis and Flight Testing of a High Altitude Synchropter UAV,” Proceedings of the Vertical Flight Society 74th Annual Forum, May 2018. DOI: 10.4050/f-0074-2018-12920.

6. Churchfield, M. J., Schreck, S. J., Martinez, L. A., Meneveau, C., and Spalart, P. R., An Advanced Actuator Line Method for Wind Energy Applications and Beyond. DOI: 10.2514/6.2017-1998.

7. Sørensen, J. N., and Shen, W. Z., “Numerical Modeling of Wind Turbine Wakes ,” Journal of Fluids Engineering, Vol. 124, (2), 05 2002, pp. 393–399. DOI: 10.1115/1.1471361.

8. Forsythe, J., Lynch, E., Polsky, S., and Spalart, P., “Coupled Flight Simulator and CFD Calculations of Ship Airwake using Kestrel:,” Vol. 2015, 01 2015. DOI: 10.2514/6.2015-0556.

9. Bauchau, O., Bottasso, C., and Nikishkov, Y., “Modeling rotorcraft dynamics with finite element multibody procedures. Math. Comput. Model. 33(10-11), 1113-1137,” Mathematical and Computer Modelling, Vol. 33, 05 2001, pp. 1113–1137. DOI: 10.1016/S0895-7177(00)00303-4.

10. Schlaffer, M. B., Non-reflecting boundary conditions for the lattice Boltzmann method, Ph.D. thesis, Technische Universität München, 2013.

11. Meldi, M., Vergnault, E., and Sagaut, P., “An arbitrary Lagrangian–Eulerian approach for the simulation of immersed moving solids with Lattice Boltzmann Method,” Journal of Computational Physics, Vol. 235, Publisher: Elsevier BV, February 2013, pp. 182–198. DOI: 10.1016/j.jcp.2012.10.014.

12. Bludau, J., “Real-time simulation of the ship-rotorcraft dynamic interface using local recalculation with the Lattice-Boltzmann method,” .

13. Horvat, B., Hajek, M., and Rauleder, J., “Computational Flight Path Analysis of a Helicopter in an Offshore Wind Farm using a Lattice-Boltzmann Method,” , 01 2021. DOI: 10.2514/6.2021-1827.